Rapid Near-Field Attenuation of Ground Motion from Shallow Induced Earthquakes, Case Study: Preston New Road, United Kingdom

Pungky M. Suroyo
Benjamin Edwards

URBASIS project

Abstract

Ground motions from shallow induced earthquakes and tectonic seismicity were investigated in this study by directly modeling the seismic attenuation quality factor (*Q*) using spectral fitting and coda envelope decay methods. We use data from the Preston New Road (PNR) shale gas induced seismicity sequences near Blackpool, United Kingdom, in 2018 and 2019, in addition to regional tectonic events in the United Kingdom. Our results show that the local *Q* obtained from the induced seismic sequences at PNR, attributed to shallower layers in the crust, leads to a rapid rate of near-field decay (sudden loss in amplitude of earthquake signal over a short distances), with significantly stronger attenuation than observed for regional events. We furthermore find that estimates of *Q* are nonunique to a given record, differing both with the method and the analysis windows used, particularly at high frequency. These differences can be attributed to the different modeling methodologies (e.g., different assumptions) or to fundamental differences in physical attenuation processes within the seismic wavefield itself, which traverses multiple ray paths and comprises various phases. Our results indicate that to model ground motions for shallow earthquakes, it is important to consider the composite *Q* along a specific path rather than an average regional *Q*. To this extent, a depth-dependent attenuation model is considered crucial to bridge the gap between shallow induced earthquakes and tectonic seismicity.

Introduction

Generally, small-magnitude earthquakes (roughly, $\mathbf{M} < 4$) do not pose a threat to people or infrastructure and are considered negligible in seismic hazard assessments (Bommer and Crowley, 2017). However, small earthquakes have become increasingly important to consider when undertaking seismic risk assessments for near-source shallow seismicity in urban environments, particularly for vulnerable building stock without earthquake-resistant design. This focus is even more important given the extent of regulatory scrutiny and public concern associated with induced seismicity. One such example is the 2.9 M_L Preston New Road (PNR) earthquake in 2019, a hydraulic fracturing triggered event in the United Kingdom. Typically, earthquakes with magnitudes <3 are barely felt, never mind damaging. However, because this event occurred at a depth of only 3 km with the epicenter only a few kilometers from the urban area of Blackpool and the wider Fylde region (~350,000 population), it was widely felt, with reports of superficial damage to buildings.

Many attempts have been made to model ground-motion resulting from induced seismicity. Typically, this involves implementing and frequently adapting pre-existing tectonic ground-motion prediction equations (GMPEs). However, using ground-motion prediction models under the assumption of similar source and attenuation characteristics to tectonic earthquakes leads to significant discrepancy between observed and predicted ground motion. For instance, a previous study carried out by Edwards *et al.* (2020, 2021) at the PNR shale gas site near Blackpool, United Kingdom, tested the performance of an existing GMPE designed for induced seismicity but based on short-distance tectonic data (Atkinson, 2015). They found that the GMPE performed satisfactorily at distances >5 km but led to significant underestimation of ground motion at shorter distances. This was because the Atkinson (2015) model did not account for sufficiently high and rapid decay of amplitudes in

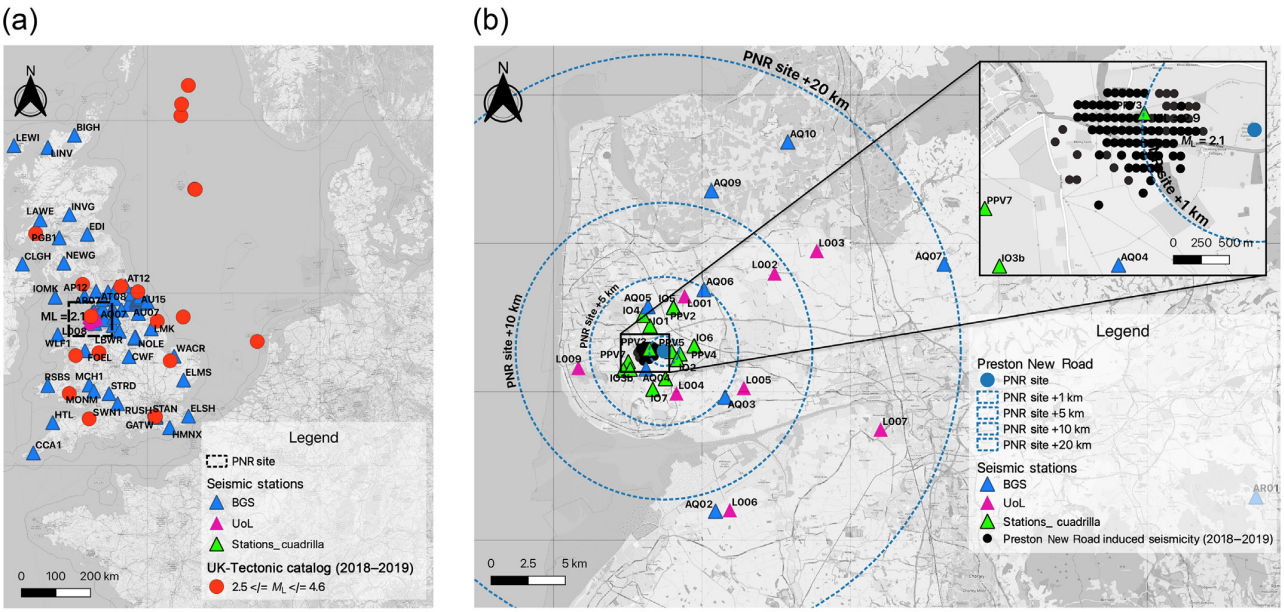

Figure 1. Map of stations and event locations (recorded in 2018–2019): (a) tectonic dataset for $2.5 \leq M_L \leq 4.6$ and (b) induced dataset from the Preston New Road (PNR) site with local magnitude range $-1.7 \leq M_L < 3$. The color version of this figure is available only in the electronic edition.

the near field. Edwards *et al.* (2021) subsequently presented a minimum-misfit, coefficient calibrated form of the Atkinson (2015) GMPE that removed the overall underestimation of motions in the near field ($R < 5$ km) by effectively increasing ground-motion amplitudes (for a given scenario) at the epicenter while simultaneously increasing the rate of attenuation before returning to the original GMPE amplitudes and rate of decay at greater distances. However, they concluded that modification of the functional form itself would be required to completely remove all fluctuations in misfit bias.

The development of a local GMPE using increasingly complex functional forms, as appears necessary to model shallow induced events, relies on the availability of sufficient data to constrain the model. In particular, a GMPE's behavior at larger magnitude, when developed using small local datasets, is often un or poorly constrained. This is why existing models, which make use of data from large datasets or multiple datasets from various sources, are typically used. The Atkinson (2015) model, for instance, is based on near source ($R < 40$ km), but not necessarily shallow, records from the Next Generation Attenuation (NGA)-West2 Project dataset, consisting of events of magnitude ≤6. It is clear that to effectively modify the functional forms of well-constrained GMPEs, we require a physical understanding of the mechanisms driving differences in ground motions. For the purpose of developing a local GMPE for induced seismicity applications, the modeling of attenuation, specific to shallow source events in the near field, is therefore one of the important factors to consider. To address this, we model and discuss the seismic attenuation of records from the PNR shale gas sequences along with regional tectonic UK events.

Common methods to quantify the physical attenuation of seismic waves, as defined by the seismic quality factor (Q), are to parameterize the spectral amplitudes of body-wave spectra (Boatwright, 1978; Hough and Anderson, 1988), to determine spectral ratios over different parts of seismograms (Aki, 1980; Frankel *et al.*, 1990) and to characterize the coda amplitude decay with increasing lapse time (Aki and Chouet, 1975), as well as methods that use collocated smaller events as empirical Green's functions (Hough, 1997). Some methods assume frequency-dependent Q, but others consider frequency-independent Q.

In this article, we use ground-motion records of induced seismicity from the PNR shale gas site along with data from recent $M_L \geq 2.5$ regional tectonic events to estimate the local and regional attenuation parameter (Q^{-1}), respectively, sing two of the most common approaches: (1) spectral fitting and (2) coda envelope decay. Finally, we compare these results with the regional UK Q_{Lg} model proposed by Sargeant and Ottemöller (2009): $Q_{Lg}(f) = 266f^{0.53}$.

Data

We analyzed two different datasets to model local (induced) and regional (tectonic) attenuation (Fig. 1). The first dataset corresponds with the induced seismicity generated by hydraulic fracturing of the Bowland Shale in northwest England between 2018 and 2019. Fracking was undertaken in two wells by Cuadrilla Resources Ltd. at PNR from 15 October to 17 December 2018 and 15 August to 6 October 2019 (wells PNR-1z, and PNR-2, respectively). The PNR site was located near Blackpool, United Kingdom, ~4 km south of Preese Hall, which was the

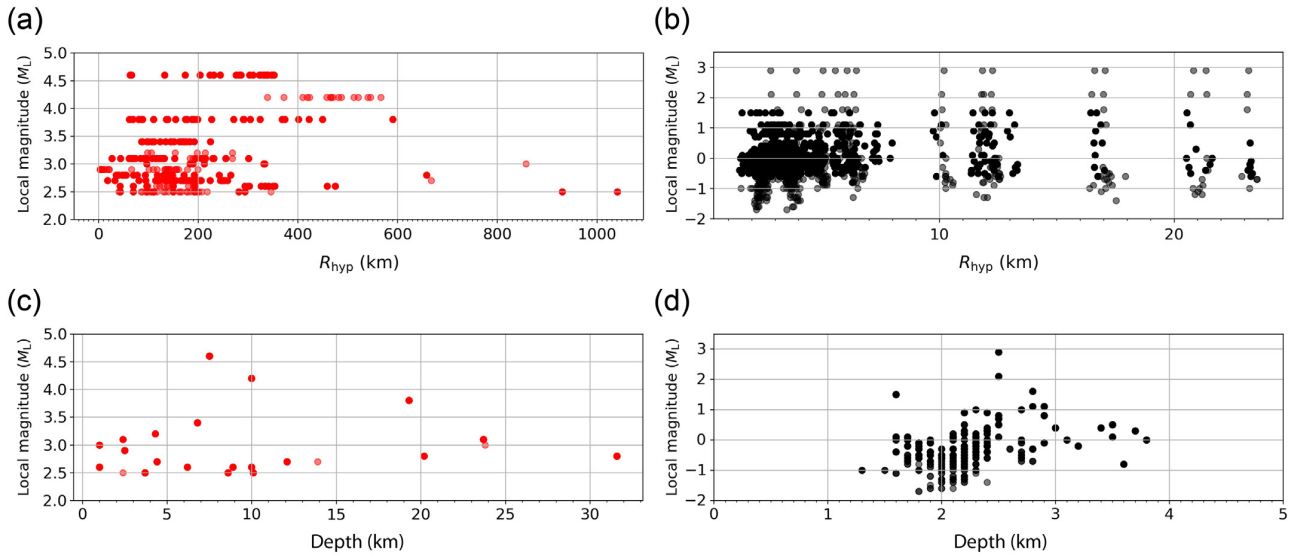

Figure 2. (a,c) Tectonic and (b,d) induced earthquake magnitude as function of (a,b) hypocentral distance and (c,d) depth. Red dots show the distribution events of the tectonic dataset, and black dots corresponds with the induced dataset. The color version of this figure is available only in the electronic edition.

first onshore shale gas site in the United Kingdom and was operated by Cuadrilla Resources in 2011. There were 192 events detected by the British Geological Survey (BGS) over both phases of seismicity during 2018–2019, with magnitudes ranging $-1.7 \le M_L \le 2.9$, recorded at hypocentral distances (R_{hyp}) <25 km (Fig. 2b). The largest event is the aforementioned 2.9 M_L PNR earthquake in 2019 (the largest hydraulic fracturing event in the United Kingdom), which was initially classified as an intensity VI EMS-98 (European Macroseismic Scale 1998) by the BGS, with Edwards *et al.* (2020, 2021) concluding that it was likely an EMS-98 intensity V event based on risk modeling and analysis of felt reports. Intensity V and VI indicate that vibration would be felt by many people, with the potential to produce superficial damage to structures.

Real-time seismic monitoring networks with high-quality broadband sensors operated by the BGS and the University of Liverpool, in addition to short-period sensors operated by Cuadrilla Resources, are used to record in three orthogonal directions (vertical and two horizontal). The dense station spacing and high-quality recordings allow the detection of very low-magnitude events ($M_L < 0$) even at the surface, with a magnitude of completeness at M_L 0.5 (Richard Luckett (BGS), personal comm., 2022).

The tectonic dataset was obtained by extending the coverage area up to 1042 km from the PNR site. Natural earthquakes in the United Kingdom are generally in the depth range 3–20 km, most at ~15 km (Musson and Sargeant, 2007; Mosca *et al.*, 2020), with almost all events $>2.5M_L$ being felt by people (Galloway, 2018). Our tectonic dataset consists of 26 regional events recorded on 51 triaxial instruments from 2018to 2019 with magnitudes ranging from $2.5 \le M_L \le 4.6$ (Fig. 2a,c). These tectonic events are recorded at a range of depths, with some exceeding 30 km, contrasting with the induced seismicity, for which events were recorded at only shallow depths (1–4 km) (Fig. 2b,d).

A standard signal processing approach is applied to both datasets and consists of removing the instrument response, detrending, tapering, and determining the noise and signal windows. The first part of windowing algorithm is to determine the arrival of *P* and *S* waves picked manually by looking at the three-component seismograms. The beginning of coda wave is defined following Perron *et al.* (2017) as $t_C = c(t_S - t_P) + t_S$, with t_S and t_P the *S*- and *P*-wave arrival time, respectively. Perron *et al.* (2017) define $c = 2.3$, which we consider valid for the regional events analyzed herein. However, adjustment was required for the induced seismicity dataset because of the very short-duration records. The modification was made by considering the relation of hypocentral distance to observed time differences between the arrival of the *S* and *P* waves, which can be expressed as follows:

$$R_{hyp} \propto 5(t_S - t_P), \tag{1}$$

in which

$$\frac{R_{hyp}}{\beta} \approx (t_S - t_0), \tag{2}$$

for an average shear-wave velocity $\beta = 3.5$ km/s, origin time t_0, and hypocentral distance (R_{hyp}). The definition of coda lapse time proposed by Aki (1969) is

$$t_C = 2(t_S - t_0) + t_0. \tag{3}$$

By substituting equation (1) into equation (2),

$$\frac{5(t_S - t_P)}{\beta = 3.5} \approx (t_S - t_0),$$

$$t_0 \approx \frac{-5(t_S - t_P)}{3.5} + t_S. \quad (4)$$

Taking the new definition of t_0 shown in the equation (4) and substituting into equation (3), the new definition of coda wave for induced events is shown in equation (5), with c = 1.4:

$$t_C = 2(t_S - t_0) + t_0,$$

$$t_C = 2\left(t_S - \left(-\frac{5(t_S - t_P)}{\beta = 3.5} + t_S\right)\right) + \left(\frac{-5(t_S - t_P)}{3.5} + t_S\right),$$

$$t_C = \left(\frac{5(t_S - t_P)}{\beta = 3.5}\right) + t_S = 1.4(t_S - t_P) + t_S. \quad (5)$$

Taking the definition of the beginning of *S* and coda waves, three different seismic windows were defined. *S*-wave window is defined as the waveform recorded from arrival of *S* wave up to the beginning of coda waves, whereas coda waves defined as the waveform from $t_C = c(t_S - t_P) + t_S$ with c = 2.3 for tectonic and c = 1.4 for induced dataset up to the end time, which corresponds to 95% cumulative energy of the whole signal. The estimation of seismic attenuation was then carried out using two different approaches detailed in the following chapter: Seismic Attenuation Measurement Methods.

Seismic Attenuation Measurement Methods

Spectral fitting method

Measurements of seismic attenuation may vary considerably when made from different parts of the seismic wavefield or using different techniques, especially at high frequencies (Sarker and Abers, 1998). In this study, the spectral analysis method detailed by Edwards *et al.* (2008) was therefore applied to three different signal windows, consisting of different contributions of the seismic wavefield: (1) the *S* wave, (2) coda window, and (3) *S* and coda (*S*+ coda) window (Fig. 3). Consistent preprocessing was applied to 8712 horizontal recordings (east–west and north–south components) of the 26 UK tectonic and 192 induced PNR events, with all records demeaned and windowed. Spectra of signal and noise windows for each record were then calculated using the multitaper method proposed by Prieto *et al.* (2009). Amplitude spectra were subsequently fitted with a model across the usable frequency range, which was defined for each recording as where the signal-to-noise ratio (SNR) is consistently (from frequency to frequency) >3. For inclusion in the spectral fitting inversion, only frequencies up to 45 Hz are considered, above which little, if any, usable signal was present.

In the fitting process, the Brune (1970) source model was assumed, which was concluded as the best-fitting source spectrum for UK events by Edwards *et al.* (2008), with the far-field displacement Fourier spectrum then expressed as follows:

$$\Omega(f) = \frac{\Omega_0 e^{-(\pi f^{1-\alpha} t^*)}}{1 + (f/f_c)^2}, \quad (6)$$

in which Ω_0 is the low-frequency spectral plateau (the signal moment), f is the frequency, f_c is the corner frequency, and t^* is the attenuation parameter ($t^* = T/Q_0$, with T the travel time and Q_0 as the path-average quality factor at the reference frequency, here 1 Hz). α describes the frequency dependence of Q, with $Q(f) = Q_0 f^{\alpha}$. The low-frequency plateau (Ω_0) term is dependent on geometrical spreading, radiation pattern effects, the seismic moment, and other frequency-independent effects, none of which are the focus of this analysis and are therefore not separated.

The path-average attenuation term t^* is subsequently defined as the integrated value of Q_0^{-1} along the ray path (R_{path}):

$$t^* = \int_{\text{path}} \frac{dR_{\text{path}}}{Q_0(R_{\text{path}})\beta(R_{\text{path}})} \simeq \frac{R_{\text{hyp}}}{Q_0\beta} + \kappa_0 = \frac{T_0}{Q_0} + \kappa_0, \quad (7)$$

in which Q_0 and T_0 is the path-average quality factor and travel time at the reference frequency, respectively. κ_0 represents the intercept at zero distance on at^* versus distance plot and therefore describes residual site-specific exponential decay (Anderson and Hough, 1984). Several recent studies (e.g., Edwards *et al.*, 2015; Ktenidou *et al.*, 2015; Mayor *et al.*, 2018; Haendel *et al.*, 2020) explained that the slope of the acceleration spectrum in log-linear space is often curved rather than linear as expected according to the Anderson and Hough (1984) kappa model. In this case, measured site-specific exponential decay (κ_0) is observed to depend on the chosen frequency band of analysis. Haendel *et al.* (2020) proposed the "zeta" model (ζ) to account for this observation. This model is therefore considered alongside the traditional κ model through a frequency dependence of κ_0 (denoted $\kappa_{0,\zeta}$) to describe any residual frequency dependence of the site-specific attenuation. In this case, the seismic spectrum in equation (6) is proportional to the attenuation term, which can be expressed as follows:

$$\Omega(f) \propto \exp\left(-\pi f \kappa_0 - \pi f^{1-\alpha}\left(\kappa_{0,\zeta} + \frac{R_{\text{hyp}}}{Q_0\beta}\right)\right), \quad (8)$$

in which β = 2.8 km/s for induced events and 3.5 km/s for tectonic events. An example of the spectral fit is shown in Figure 4.

The spectral inversion is performed for each individual recording following the steps in Figure 5 to fit t^*, f_c, Ω_0, and α (with a grid search in the range 0–1), which allows us to calculate both frequency-dependent and frequency-independent Q measurements. The fitting was performed under the assumption that different records from a single event will have the same seismic moment and Brune stress drop and therefore are fitted to an event-specific corner frequency (f_c). Although we acknowledge that corner frequency may vary slightly as a function of azimuth (e.g., Madariaga, 1976), we

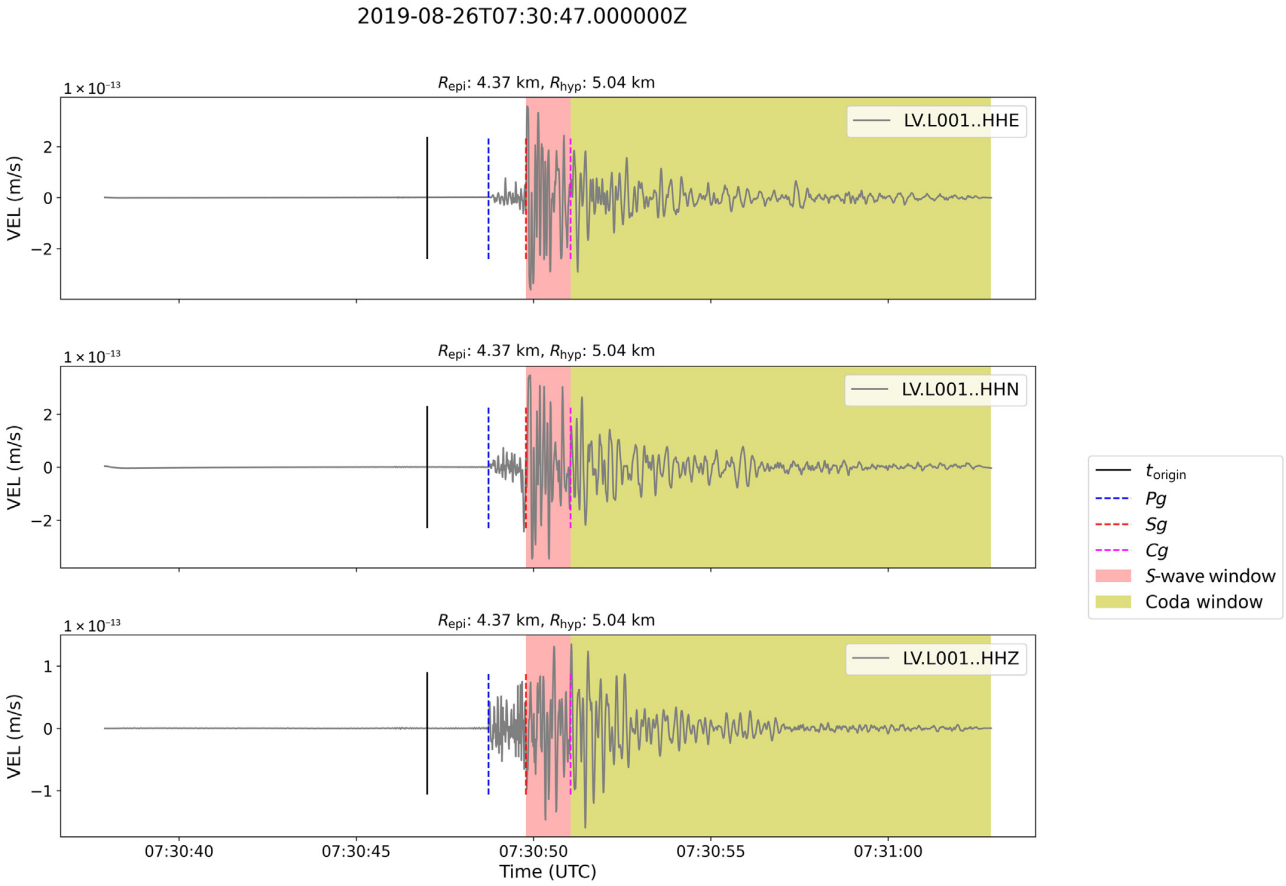

Figure 3. Example of time series, *S* wave, and coda window for the PNR dataset event: 26 August 2019 T07:30:47.0 recorded in sensor LV.L001. The arrival of the *P* wave (*Pg*), *S* wave (*Sg*), and coda wave (*Cg*) is shown by the dashed lines, and the origin time of the earthquake (t_{origin}) is shown by the black line. The color version of this figure is available only in the electronic edition.

do not consider such deviations resolvable with this approach. The inversion scheme is divided into two main steps:

First inversion step: the main objectives of this stage are (1) finding the optimum frequency dependence of Q_0, α (i.e., α that corresponds with the minimum chi-squared $[X_i^2]$ misfit, denoted as α_{min}) and (2) fixing $\alpha = 0$ to calculate the frequency-independent Q_0 and κ_0. To find the frequency dependence of Q_0 (α_{min}), the chi-squared (X_i^2) misfit over the log spectral amplitudes for α within the range 0.0–1.0 were calculated. In this way, the model misfit over the ensemble of observations for each given α can be quantified. An interval of α_{min} was calculated using bootstrap method by resampling the dataset with replacement (20% repetition and 80% retention). Bootstrap samples from the original dataset were generated by random selection and the corresponding α_{min} from 15,000 resamples determined. The mean of α_{min} and its lower and upper limits were then estimated, as shown in Figure 6. A frequency-independent model (Q_0 and κ_0) was also determined using linear regression of t^* versus R_{hyp} for a given $\alpha = 0$.

Second inversion step: this step was performed by fixing various elements based on the previous inversion results. A correction for frequency-independent κ_0 is applied, and the final inversion performed using a grid search over f_c between 0 and 50 Hz, fixing discrete selections of α_{min} (lower limit of α_{min}: upper limit of α_{min}). Another bootstrap analysis was performed to a linear regression of t^* versus R_{hyp} for each iteration (Fig. 7). A parametric bootstrap analysis was carried out with 100 iterations, each fitted with a linear regression and retaining the intercept and slope coefficients. The product of the second inversion is then the final $Q(f)$ and frequency-dependent $\kappa_{0,\zeta}$ model (i.e.,Q_0, α, κ_0, and $\kappa_{0,\zeta}$), which can subsequently be used for determining seismic source parameters.

Coda envelope decay method

The coda envelope decay method is an alternative approach to modeling seismic attenuation. The method takes advantage of the scattered seismic wavefield, which manifests as coda waves in the seismogram. The coda is assumed to be caused by the scattering of body waves by heterogeneities distributed randomly in the upper part of the Earth (Aki, 1969; Aki and Chouet, 1975). An important factor to consider while implementing this

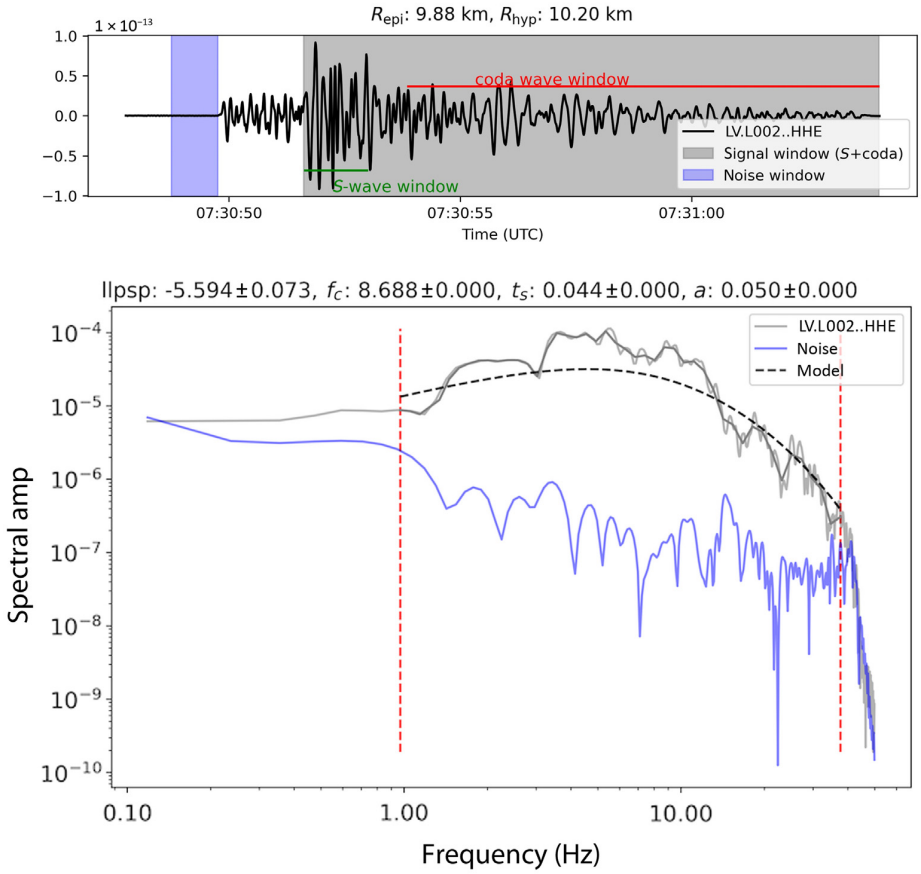

Figure 4. Example of signal (S+ coda wave) spectra (gray line) fitted with the model (black dashed line) and noise spectra (blue line). The upper and lower frequency bounds shown by the red dashed line were computed based on the signal-to-noise ratio (SNR > 3). The color version of this figure is available only in the electronic edition.

technique is that a long enough coda window is available to observe the envelope decay.

The coda-wave amplitude (A) at frequency (f) and lapse time (t) or time from the event origin is described by

$$A(f,t) = A_0(f)t^{-\nu}e^{-\pi f t/Q_{Clt}}, \tag{9}$$

in which A_0 is the initial amplitude, f is the frequency, t is the lapse time from the origin time, ν is a positive constant that is related to geometrical spreading (Aki and Chouet, 1975), and Q_{Clt} is the quality factor for coda waves calculated using the coda envelope decay method. The positive constant (ν) can be assumed as either multiscattering or single scattering. In this study, we assumed the single scatter model ($\nu = 1$), which corresponds to scatter of S waves.

Calculations of the Q-value were carried out for both tectonic and induced seismicity datasets using all three components (two horizontal and one vertical component). Only the good coda signal (SNR > 2) is subsequently considered in the calculations.

The calculation of the decay of coda energy is estimated at discrete frequencies; therefore, we first filter the seismogram with a set of narrowband filters centered on discrete frequencies. In this study, 10 central frequencies (f_{cen}) were used with lower frequency $f_{low} = 10$ Hz and upper frequency $f_{up} = 25$ Hz for the PNR dataset and $f_{low} = 3$ Hz, $f_{up} = 15$ Hz for the UK tectonic dataset, corresponding to the dominant usable frequency ranges in the respective datasets:

$$f_{cen} = f_{low}\left(\frac{f_{up}}{f_{low}}\right)^{\frac{i-1}{10}}, \quad i = 1,2,\ldots,10. \tag{10}$$

The bandwidth of filters was chosen to be constant in logarithmic scale in which the upper and lower limit of frequency band calculated using the Finite Impulse Response (FIR) filter method by Oppenheim and Schafer (1975). This method determines upper and lower frequency limits by calculating the corresponding duration window (T_{WN}) as a function of the central frequency (f_{cen}), expressed as follows:

$$T_{WN} = \frac{3}{2f_{cen}}. \tag{11}$$

Frequency ranges used in the band-pass filter for both induced and tectonic datasets are presented in Table 1. The instantaneous power of these filtered signals is estimated from modulus of the analytical signal or envelope of coda by taking logarithm of the Hilbert transform of $A(f,t)$. The slope of the amplitude decay is then determined using linear least-squares regression (Fig. 8). This can subsequently be used to calculate the quality factor at each discrete frequency for each individual record. The average of quality factor from all different stations is then calculated and presented as the final model of the dataset $[Q_{Clt}(\frac{f}{f_r})^{\alpha}]$.

Results and Discussion

To model the seismic attenuation quality factor ($Q(f) = Q_0 f^a$), spectral fitting was performed following the inversion

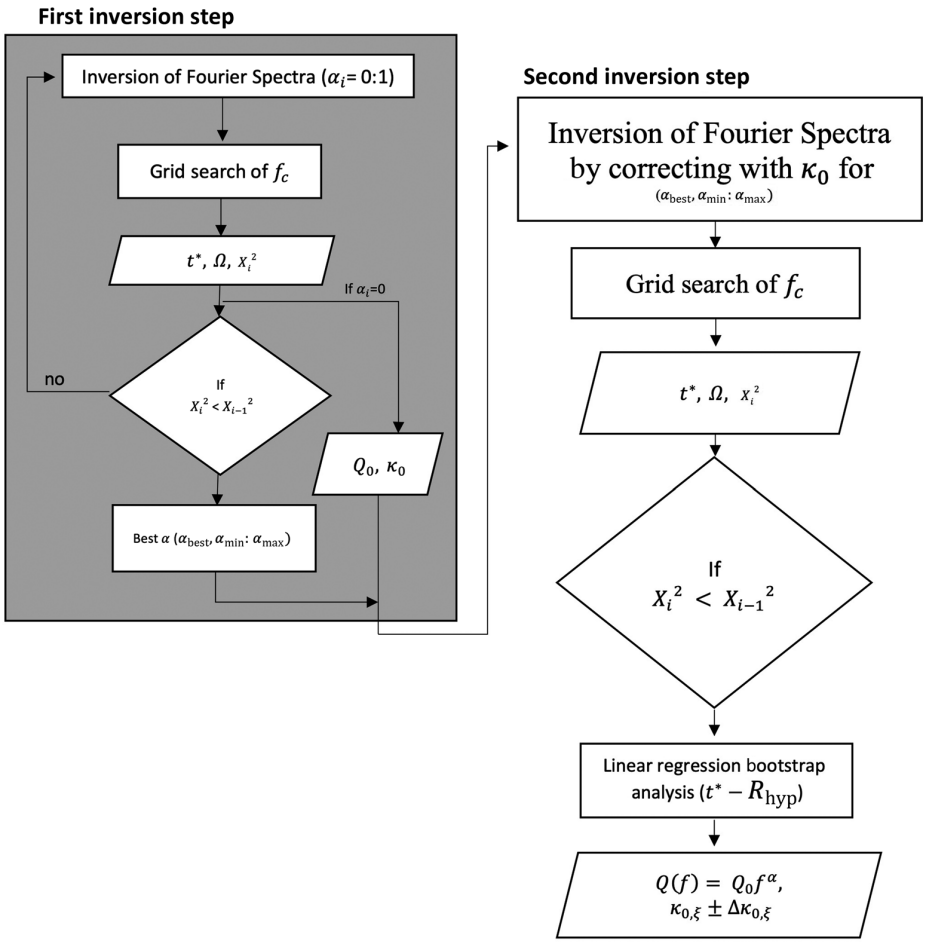

Figure 5. Flowchart of inversion process for the spectral fitting method.

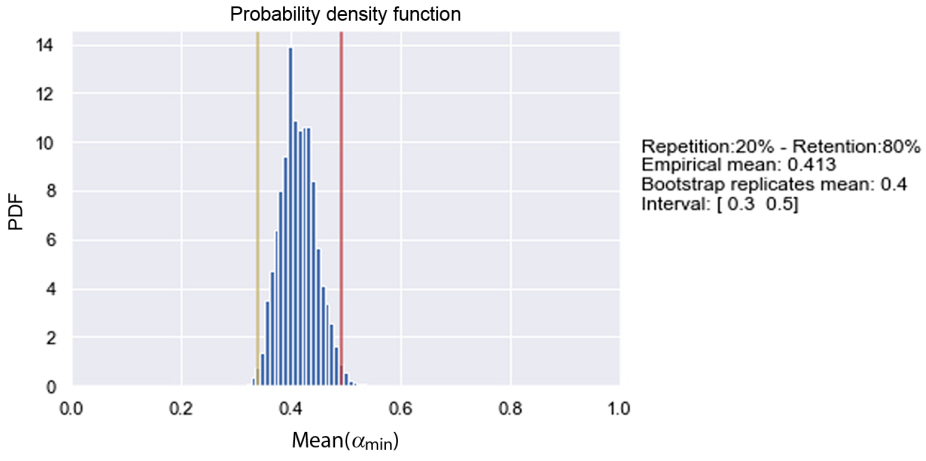

Figure 6. Lower (yellow line) and upper (red line) limits values that correspond to the minimum and maximum mean of α_{min} bootstrap replicate for α([0 : 1]) from the spectral fitting of the *S* wave from the tectonic dataset. α_{min} defined as the mean of α_{min} between 0.3 and 0.5. The color version of this figure is available only in the electronic edition.

scheme explained in the previous section. Q_0 is determined for both induced and regional events in terms of best fit and interval for the three seismogram windows. Q models from the induced PNR datasets, based on the results using *S* wave, coda wave, and *S*+ coda-wave windows, respectively, are $Q_S = 108.2f^{0.15}$, $Q_{S+coda} = 144.1f^{0.05}$, $Q_c = 203.5f^{0.10}$. Results from the regional tectonic dataset led to $Q_S = 678.3f^{0.40}$, $Q_{S+coda} = 171.9f^{0.60}$, and $Q_c = 142.4f^{0.65}$ (Fig. 9). The confidence intervals of each model are presented in Figure 9. The confidence interval of each model represents the Q_{min} and Q_{max}, inverted from upper and lower values of α_{min}, respectively, as obtained from the first step of inversion scheme. Two initial observations can be made from these analyses: first, the Q models for regional tectonic data exhibit a consistently higher exponential variable (α), compared with Q from induced events, which we propose is due to stronger scattering effects observed for records of tectonic seismicity, and, more generally, the more complex paths taken by the myriad phases within the regional wavefield. Attenuation models for induced (near-source distance) events, on the other hand, tend to be frequency independent and dominated by intrinsic attenuation. The second observation is that the average attenuation, over a range of moderate to high frequency, is significantly higher for the shallow induced events (Fig. 9).

Looking in more detail at the results from tectonic data, we note that for the body-wave quality factor Q_S we observe a

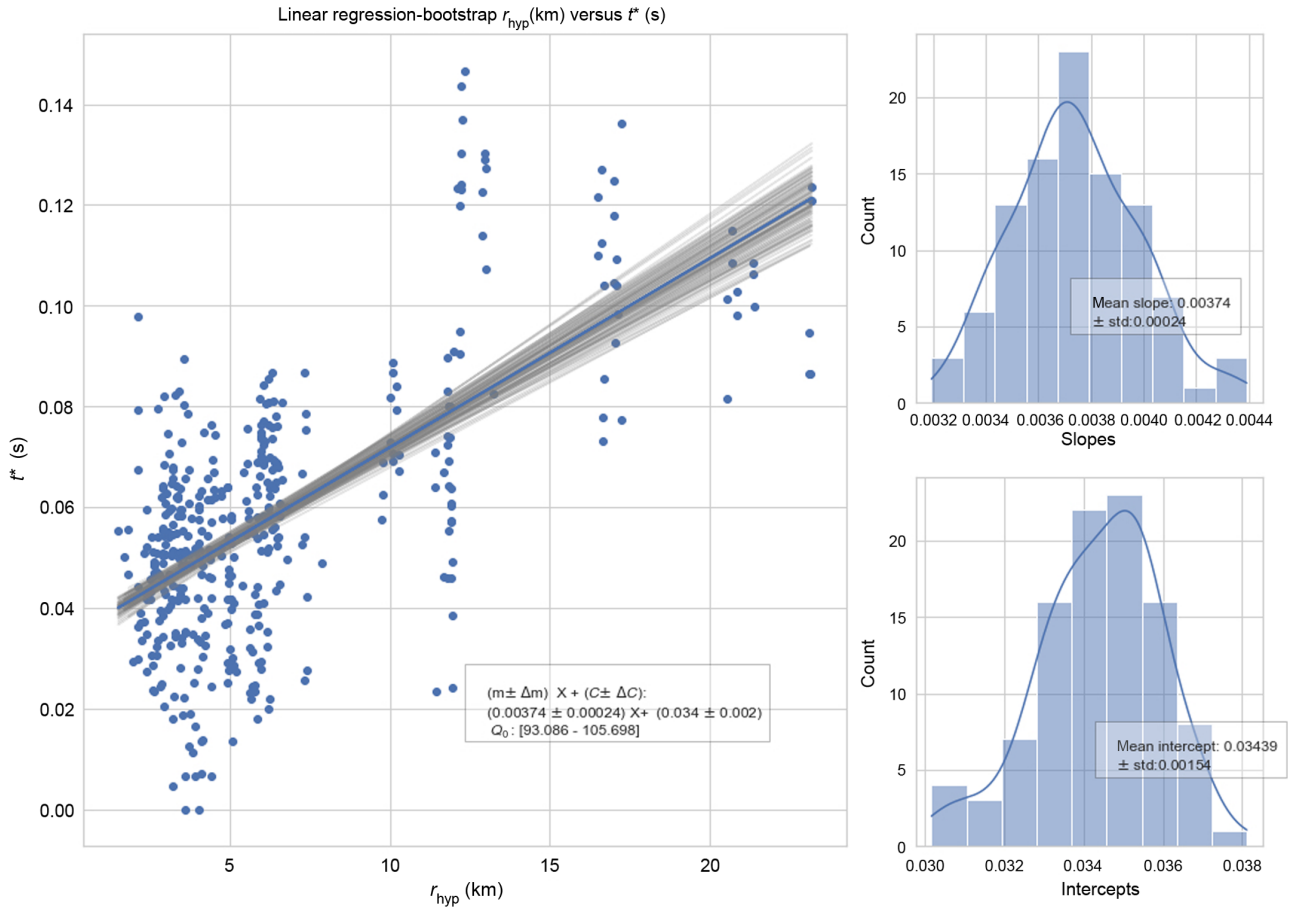

Figure 7. Example of bootstrapping regression t^* versus R_{hyp}. Range of Q_0 defined as $1/(\beta \times (m \pm \Delta m))$, in which β is shear-wave velocity in meters per second and m is the slope of linear regression. Intercept of the linear regression $C \pm \Delta C$ represents the residual site-specific exponential decay ($\kappa_0 \pm \Delta\kappa_0$). The color version of this figure is available only in the electronic edition.

significantly higher reference Q_0 (678) than for Q_c (172) and Q_{S+coda} (142), suggesting that, at least for the lower frequencies of those under analysis, the body waves propagate much more efficiently than coda. This is consistent with the understanding that *S* waves at regional distances propagate into deeper crust, whereas coda waves are most likely accompanied by scattered waves and dominate in the upper and therefore lower-velocity layers. As a result of the more complex wavefield path, the records of tectonic events therefore exhibit more pronounced within-wavefield variation in attenuation than those for induced events. Differences in the volume sampled by different seismic windows (*S* wave, coda wave, or *S*+ coda wave) can therefore affect the frequency dependence of *Q*.

The coda envelope decay method was performed to focus on the scattering effect that manifests in the tail of the wavefield. This method is sensitive to the selection of time windows and filter bandwidth. In this study, the coda envelope decay is implemented for individual recordings over all components $[Q_{Clt(i)}(f)]$ and defined at 10 central frequencies. The final *Q* model for each dataset is estimated by taking the mean of *Q* at a reference frequency, in this case the lower frequency bound for the respective datasets: 10 Hz for the induced dataset and 3 Hz for the tectonic. We find $Q_{Clt}(f) = 121.6(f/10)^{1.18}$ for the induced dataset, systematically lower than *Q* for the tectonic dataset, in which $Q_{Clt}(f) = 262.2(f/3)^{0.95}$. The higher frequency dependency of *Q* observed in the time-domain coda envelope analysis is related to the depth penetration of the high- (shallow) and low-frequency (deep) coda wave. Any changes of *Q* with depth are mapped into an apparent frequency dependence of *Q*. At higher frequencies, the coda wave is suspected to be related to surface scatters which rapidly attenuate. The observation from coda envelope decay analyses is difficult to compare with the *Q* modeled from spectral fitting approach. In particular, methodological constraints should be considered: the *Q* estimates require correction for geometrical spreading when using the coda envelope decay method, whereas in the spectral fitting approach, no such correction is required (geometrical spreading does not change the shape of spectra).

Even though the frequency dependencies of *Q* models are suspected as a compensation of the distance and depth (path)

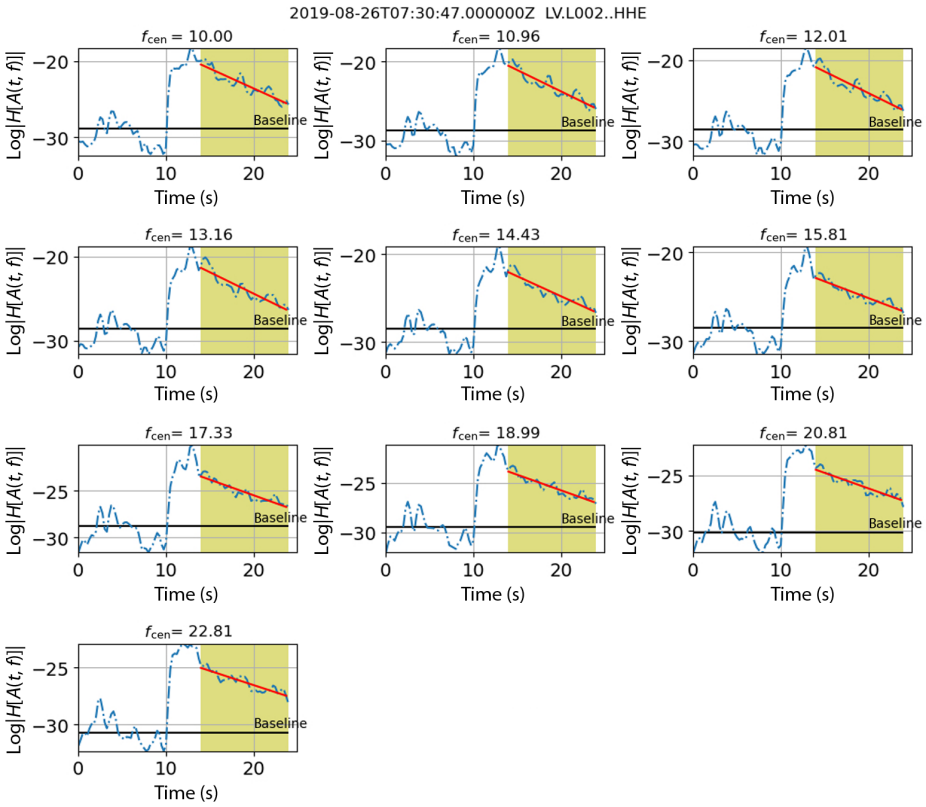

Figure 8. Example of spectra fitting (left), and coda envelopes ($log(|[A(f,t)]|)$) as well as linear regression $Q_{Clt}(f)$ (red lines) for 10 different central frequencies in bands (10–25 Hz) (right) for the PNR dataset event: 26 August 2019 T07:30:47.0 recorded in sensor LV.L002 (east–west component). Noise baseline showed as black line and coda windows displayed as yellow rectangle. The color version of this figure is available only in the electronic edition.

dependence of Q, the true cause of the frequency dependencies of Q remains poorly understood. In the case of induced seismicity, the Q model (spectral fitting result) shows a lower α and becomes frequency independent, which suggests that the propagation is dominated by intrinsic attenuation. Another explanation for the lower α found in the induced seismicity is that when the scattering on small-scale heterogeneities cannot be clearly isolated, it possibly includes both intrinsic and scattering attenuation. In this case, the attenuation can be described as a purely geometrical, frequency independent, process of amplitude decay that might occur either by spreading or scattering of seismic waves (Morozov, 2008). Values of $\alpha > 1$ (as found in coda envelope decay analysis for induced seismicity) can be interpreted as the decreasing of the efficiency of scattering at shorter scale distance

TABLE 1
Frequency Ranges in Band-Pass Filter for the Coda Envelope Decay Method

	Induced Dataset				**Tectonic Dataset**			
Number	f_{cen}	T_{WN}	$f_{band_{low}}$	f_{band_upper}	f_{cen}	T_{WN}	f_{band_low}	f_{band_upper}
1	10	0.15	6.67	13.33	3	0.5	2	4
2	10.96	0.14	7.31	14.62	3.52	0.43	2.35	4.69
3	12.01	0.13	8.01	16.02	4.14	0.36	2.76	5.52
4	13.16	0.11	8.76	17.55	4.86	0.31	3.24	6.48
5	14.43	0.10	9.62	19.24	5.71	0.26	3.80	7.61
6	15.81	0.09	10.54	21.08	6.71	0.22	4.47	8.94
7	17.33	0.08	11.55	23.10	7.88	0.19	5.25	10.51
8	18.99	0.78	12.66	25.32	9.26	0.16	6.17	12.34
9	20.81	0.07	13.88	27.75	10.87	0.14	7.25	14.49
10	22.81	0.06	15.21	30.41	12.77	0.11	8.51	17.03

f_{cen}, central frequency; T_{WN}, duration window; f_{band_low}, lower frequency band; f_{band_upper}, upper frequency band.

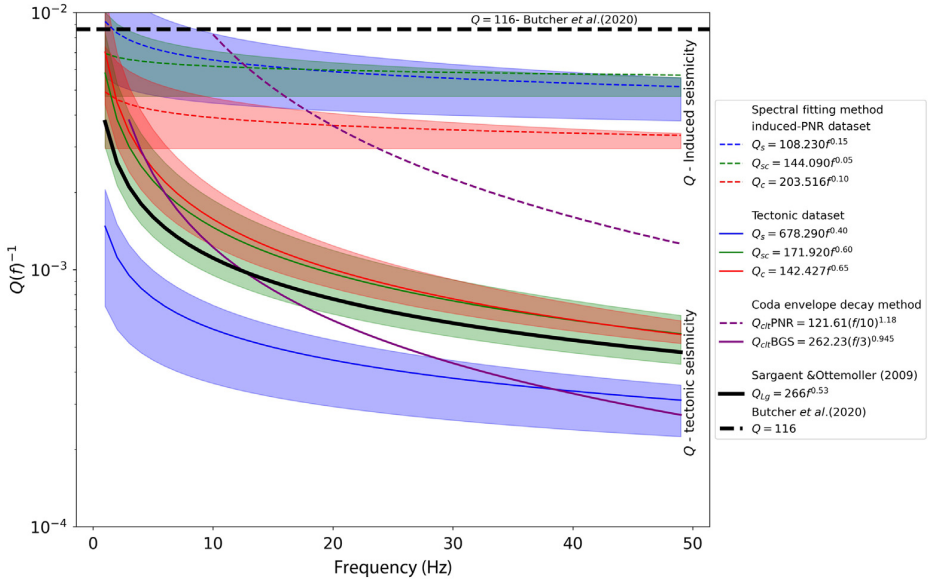

Figure 9. Attenuation model from spectral fitting and coda envelope decay method for the induced and tectonic datasets. The shaded color shows the confidence interval of the Q model. The color version of this figure is available only in the electronic edition.

(Morozov, 2008). Relying on this interpretation of α and the lower overall Q (stronger attenuation) for induced seismicity, it implies a rapid attenuation at short distances (Fig. 10). Although somewhat counter-intuitive, this can explain the underprediction of very near-field ground motions by GMPEs for small to moderate shallow events: in considering only observations at "typical" distances available in ground-motion datasets (R > ~5 km) and extrapolating back toward the epicenter, without considering a sufficiently rapid rate of attenuation, we underestimate epicentral ground-motion amplitudes.

Another study about Q estimation from shallow swarm-like seismicity in the United Kingdom was carried out by Butcher *et al.* (2020) using 305 seismic events with magnitudes ranging between $-0.7 < M_L < 2.1$ recorded from seven broadband seismometers installed to investigate mining-induced seismicity. The authors reported frequency-independent $Q = 116 \pm 23$, whereas κ_0 was evaluated from noise signals ($\kappa_{0-noise}$) and ranged between 0.022 and 0.034 s, with standard deviations between 0.006 and 0.009. These results show slightly lower Q and higher κ_0 compared with our results for induced seismicity at PNR (see Table 2). The order of magnitude is nevertheless consistent with the induced seismicity results rather than the tectonic results. The small differences between the results of our study and Butcher *et al.* (2020) may be expected because of different local geology. Finally, the regional Q estimated in this study, especially Q modeled using spectral

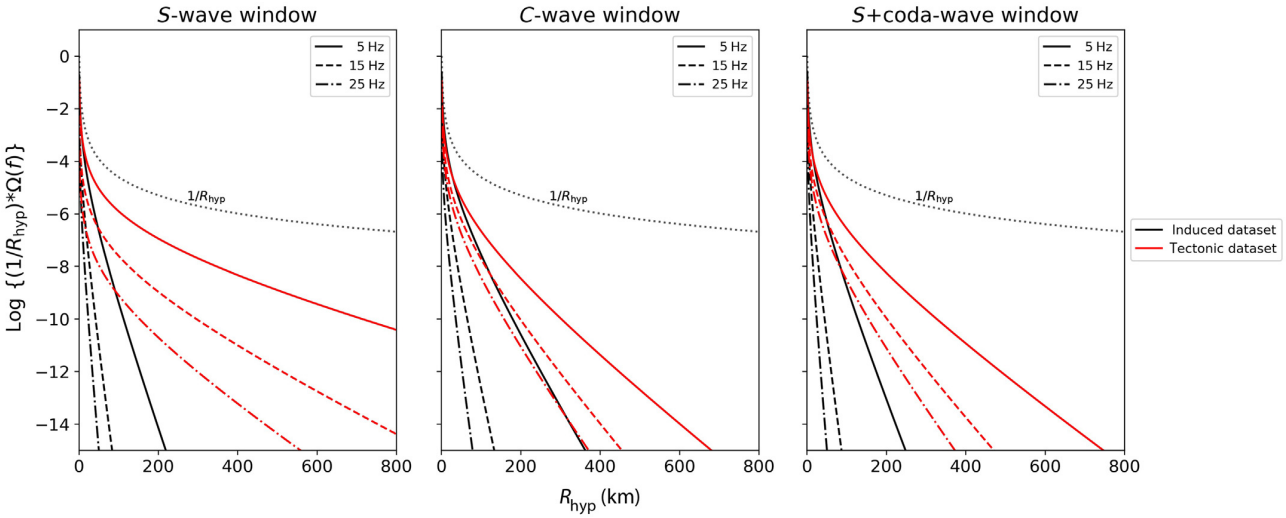

Figure 10. Spectral attenuation model as a function of distance at different frequencies (5, 15, and 25 Hz) for the tectonic (red) and induced (black) datasets. R^{-1} decay is shown by the gray dashed lines. The color version of this figure is available only in the electronic edition.

TABLE 2
Q_0(1 Hz), α, $\kappa_{0,\zeta(1\ Hz)}$, and κ_0 from Spectral Fitting Method (Results for Frequency-Dependent and Frequency-Independent Models from Three Different Signal Windows)

		Frequency-Dependent Model, Final Model after Corrected with κ_0 (Second Inversion)				Frequency-Independent Model (Initial Inversion; α= 0)	
	Signal Window	**$\alpha \pm \Delta\alpha$**	**Q_0 Interval**	**$Q(f) = Q_0 f^{\alpha}$**	**$\kappa_{0,\zeta \pm \Delta\kappa_{0,\zeta}}$(s)**	**Q_0**	**$\kappa_0 \pm \Delta\kappa_0$(s)**
Induced dataset (Preston New Road)	*S* wave	0.15 ± 0.1	[67.84–178.56]	$108.23\ f^{0.15}$	0.033 ± 0.0013	169.63	0.018 ± 0.001
	S+ coda wave	0.05 ± 0.1	[99.79–211.78]	$144.098f^{0.05}$	0.018 ± 0.00125	172.46	0.019 ± 0.001
	Coda wave	0.1 ± 0.1	[135.49–338.14]	$203.52f^{0.1}$	0.021 ± 0.0016	246.11	0.020 ± 0.001
Tectonic dataset	*S* wave	0.4 ± 0.1	[487.84–1387.99]	$678.29f^{0.4}$	0.06 ± 0.012	2953.98	0.029 ± 0.003
	S+ coda wave	0.6 ± 0.1	[119.99–332.84]	$171.92f^{0.6}$	0.15 ± 0.024	1745.36	0.004 ± 0.002
	Coda wave	0.65 ± 0.1	[85.25–227.7]	$142.43f^{0.65}$	0.16 ± 0.032	2055.32	0.004 ± 0.002

Q_0, quality factor at reference frequency (1 Hz); α, frequency dependence of attenuation quality factor (Q) and its standard deviation ($\Delta\alpha$); $\kappa_{0,\zeta}$, frequency dependence of κ_0 and its standard deviation $\Delta\kappa_{0,\zeta}$; κ_0, classic kappa or residual site-specific exponential decay at zero distance (Anderson and Hough, 1984) and its standard deviation ($\Delta\kappa_0$).

fitting of *S*+ coda wave ($Q_{S+\mathrm{coda}}(f) = 171.9f^{0.60}$), gives the closest result to the regional Q model of Britain proposed by Sargeant and Ottemöller (2009), which was determined between 1 and 10 Hz for regionally propagating *Lg* waves ($266f^{0.53}$). This similarity (Fig. 9) is likely due to the possibility of sampling the same crustal volume. Our findings therefore justify that the local Q obtained from the induced seismic sequences, such as those at PNR attributed to shallower layers in the crust leads to significantly stronger and less frequency-dependent attenuation than for regional events. The unaccounted rapid decay at short distance can provide explanation of greater ground-motion amplitudes observed at short distances (Luckett *et al.*, 2019; Edwards *et al.*, 2021) than those predicted by GMPEs, which are typically calibrated at longer distances and assume that (nonrapid) attenuation can be simply extrapolated back to the source. We suggest that rapid loss of ground-motion amplitude at very near distances therefore needs to be considered in developing or adjusting GMPEs for induced seismicity.

Conclusions

In summary, this study demonstrates stronger attenuation of ground motions for near-source shallow earthquakes in the United Kingdom by comparing the seismic quality factor (Q) for the UK region and for an induced seismicity sequence at the PNR shale gas site, Blackpool, United Kingdom. Our results show that Q is nonunique to a given record but rather depends on the analysis windows (and method) used, particularly at high frequencies. The lower overall Q (stronger attenuation) in the induced seismicity and the decreasing of the efficiency of scattering effect at short-scale distance justifies that directly adapting tectonic GMPE for induced seismicity will produce bias. Therefore, to predict ground-motion models for shallow earthquakes, it is important to consider the rapid rate of attenuation observed at very near distances. This study also observed that Q might vary with the increase of depths captured by the apparent frequency dependence of Q. Hence, using the average of Q along a specific path (which will depend on, for instance, source depth) is suggested to better develop new GMPEs for induced seismicity instead of using average regional Q. Modeling an effective Q to resolve the time and depth-dependent scattering and attenuation properties is proposed for future development.

Data and Resources

The earthquake catalog for Preston New Road (PNR) dataset and tectonic dataset is available at the British Geological Survey (BGS) earthquake database (http://www.quakes.bgs.ac.uk/earthquakes/dataSearch.html, last accessed December 2020). Seismic waveform data used in this study are available on request from the BGS and operator data and University of Liverpool (UoL data).

Acknowledgments

Parts of the code used for processing and modeling seismic spectra in this study were provided by James Holt (2019). The authors wish to express their gratitude to URBASIS–EU Project members and Early Stage Researchers for their helpful comments.

References

Aki, K. (1969). Analysis of the seismic coda of local earthquakes as scattered waves, *J. Geophys. Res.* **74,** 615–631.

Aki, K. (1980). Attenuation of shear-waves in the lithosphere for frequencies from 0.05 to 25 Hz, *Phys. Earth Planet. In.* **21,** 50–60.

Aki, K., and B. Chouet (1975). Origin of coda waves; source, attenuation and scattering effects, *J. Geophys. Res.* **80,** 3322–3342.

Anderson, J. G., and S. Hough (1984). A model for the shape of the Fourier amplitude spectrum of acceleration at high frequencies, *Bull. Seismol. Soc. Am.* **74,** 1969–1994.

Atkinson, G. M. (2015). Ground-motion prediction equation for small-to-moderate events at short hypocentral distances, with application to induced-seismicity hazards, *Bull. Seismol. Soc. Am.* **105,** no. 2A, 981–992.

Boatwright, J. (1978). Detailed spectral analysis of two small New York state earthquakes, *Bull. Seismol. Soc. Am.* **68,** 1117–1131.

Bommer, J. J., and H. Crowley (2017). The purpose and definition of the minimum magnitude limit in PSHA calculations, *Seismol. Res. Lett.* **88,** no. 4, 1097–1106.

Brune, J. (1970). Tectonic stress and the spectra of seismic shear waves from earthquakes, *J. Geophys. Res.* **75,** no. 26, 4997–5009.

Butcher, A., R. Luckett, J. Kendall, and B. Baptie (2020). Seismic magnitudes, corner frequencies, and microseismicity: Using ambient noise to correct for high-frequency attenuation. *Bull. Seismol. Soc. Am.* **110,** no. 3, 1260–1275.

Edwards, B., H. Crowley, and R. Pinho (2020). *Final report on: "WP2-impacts of seismicity: Transmission to people, property and well integrity"*, Technical report, intraseis.ltd, Report number: ISEIS-HC-RP-JJB-OGA_WP2-8-22-07-2020.

Edwards, B., H. Crowley, R. Pinho, and J. J. Bommer (2021). Seismic hazard and risk due to induced earthquakes at a shale gas site, *Bull. Seismol. Soc. Am.* **111,** no. 2, 875–897, doi: 10.1785/0120200234.

Edwards, B., T. Kraft, C. Cauzzi, P. Kästli, and S. Wiemer (2015). Seismic monitoring and analysis of deep geothermal projects in St Gallen and Basel, Switzerland, *Geophys. J. Int.* **201,** no. 2, 1022–1039.

Edwards, B., A. Rietbrock, J. J. Bommer, and B. Baptie (2008). The acquisition of source, path, and site effects from microearthquake recordings using Q tomography: Application to the United Kingdom, *Bull. Seismol. Soc. Am.* **98,** 1915–1935, doi: 10.1785/0120070127.

Frankel, A., A. McGarr, J. Bicknell, J. Mori, L. Seeber, and E. Cranswick (1990). Attenuation of high-frequency shear waves in the crust: Measurements from New York state, South Africa, and Southern California, *J. Geophys. Res.* **95,** 17,441–17,457.

Galloway, D. D. (2018). The Bulletin of British Earthquakes 2016, *British Geol. Surv. Open-File Rept.*, OR/18/019, available at http://www.earthquakes.bgs.ac.uk/publications/bulletins/2018_EQ_Bulletin.pdf (last accessed May 2022).

Haendel, A., J. G. Anderson, M. Pilz, and F. Cotton (2020). A frequency-dependent model for the shape of the Fourier amplitude spectrum of acceleration at high frequencies, *Bull. Seismol. Soc. Am.* **110,** no. 6, 2743–2754, doi: 10.1785/0120200118.

Hough, S. E. (1997). Empirical green's function analysis: Taking the next step, *J. Geophys. Res.* **102,** 5369–5384.

Hough, S. E., and J. G. Anderson (1988). High-frequency spectra observed at Anza, California: Implications for Q structure, *Bull. Seismol. Soc. Am.* **78,** 692–707.

Ktenidou, O.-J., N. A. Abrahamson, S. Drouet, and F. Cotton (2015). Understanding the physics of kappa (κ): Insights from a downhole array, *Geophys. J. Int.* **203,** no. 1, 678–691.

Luckett, R., L. Ottemöller, A. Butcher, and B. Baptie (2019). Extending local magnitude M_L to short distances, *Geophys. J. Int.* **216,** no. 2, 1145–1156, doi: 10.1093/gji/ggy484.

Madariaga, R. (1976). Dynamics of an expanding circular fault, *Bull. Seismol. Soc. Am.* **66,** no. 3, 639–666.

Mayor, J., S. S. Bora, and F. Cotton (2018). Capturing regional variations of hard-rock κ_0 from coda analysis, *Bull. Seismol. Soc. Am.* **108,** no. 1, 399–408.

Morozov, I. B. (2008). Geometrical attenuation, frequency dependence of *Q*, and the absorption band problem, *Geophys. J. Int.* **175,** 239–252, doi: 10.1111/j.1365-246X.2008.0388.x.

Mosca, I., S. Sargeant, B. Baptie, R. M. W. Musson, and T. Pharaoh (2020). National seismic hazard maps for the UK: 2020 update, *British Geol. Surv. Open-File Rept.* OR/20/053, 138 pp.

Musson, R. M. W., and S. Sargeant (2007). Eurocode 8 seismic hazard zoning maps for the UK, British Geological Survey Technical Report CR/07/125, Issue 3.0, United Kingdom.

Oppenheim, A. V., and R. W. Schafer (1975). *Digital Signal Processing Practice*, Hall International Inc., Tonbridge, United Kingdom, 1227–1296.

Perron, V., A. Laurendeau, F. Hollender, P.-Y. Bard, C. Gélis, P. Traversa, and S. Drouet (2017). Selecting time windows of seismic phases and noise for engineering seismology applications: A versatile methodology and algorithm, *Bull. Earthq. Eng.* **16,** 2211–2225.

Prieto, G. A., R. Parker, and F. Vernon (2009). A Fortran 90 library for multitaper spectrum analysis, *Comput. Geosci.* **35,** 1701–1710.

Sargeant, S., and L. Ottemöller (2009). *Lg* wave attenuation in Britain, *Geophys. J. Int.* **179,** no. 3, 1593–1606.

Sarker, G., and G. Abers (1998). Comparison of seismic body wave and coda wave measures of Q, *Pure Appl. Geophys.* **153,** 665–683, doi: 10.1007/s000240050213.